# A Tristate Rigid Reversible and Non-Back-Drivable Active Docking Mechanism for Modular Robotics

Paul M. Moubarak, *Student Member, IEEE*, and Pinhas Ben-Tzvi, *Senior Member, IEEE*

***Abstract*—This paper proposes a new active bonding mechanism that achieves rigid, reversible, and nonback-drivable coupling between modular mobile robots in a chain formation. The first merit of this interface lies in its ability to operate in three independent modes. In the *drive mode*, the motor torque is routed to drive the module. In the *clamp mode*, the motor torque is redirected toward an active joint that enables one module to rotate relative to its neighbors in the formation. In the *neutral mode*, the motor's rotation achieves alignment between the interface's components prior to the initiation of the *drive* and *clamp* modes. The second merit stems from the dual-rod slider rocker (DRSR) mechanism, which toggles between the interface's three modes of operation. The design details of the interface are presented, as well as the optimal kinematic synthesis and dynamic analysis of the DRSR mechanism. Simulation and experimental results validate the DRSR's unique kinematics, as well as the rigidity and the three operation modes of the docking interface.**

***Index Terms*—Active docking, dual-rod slider-rocker mechanism (DRSR), modular robotics, multiobjective optimization.**

TABLE I
SAMPLE OF EXISTING MODULAR ROBOTS WITH THEIR RESPECTIVE DOCKING INTERFACES

| Robot Name | Year | Docking Interface |
|---|---|---|
| POLYBOT [17] | 1998 | SMA latching connectors |
| Crystalline [18] | 1999 | Mechanical latching connectors |
| I-Cubes [19] | 2000 | Interconnecting links |
| M-TRAN I, II [20] | 2002 | Permanent magnets and SMA detaching mechanism |
| Millibots [21] | 2002 | SMA actuated latches |
| Uni-Rover [22] | 2002 | Robotic grippers |
| ATRON [23] | 2003 | Electromechanical connectors |
| SuperBot [24] | 2004 | Mechanical connectors |
| Catoms [25] | 2005 | Electromagnets |
| Molecubes [26] | 2005 | Permanent and electro magnets |
| S-Bots [27] | 2006 | Robotic gripper |
| AMOEBA-I [28] | 2006 | Link-type interface |
| CKBot [29] | 2007 | Magnetic docking interface |
| iMobot [30] | 2010 | Manually connected faceplates |

## I. INTRODUCTION

SHAPE metamorphosis in modular robotics refers to the process of coupling multiple agents of a swarm into a formation that augments the capabilities of the individual module. The chain or lattice architectures [1], [2] resulting from manual or autonomous reconfiguration [3], [4] enable the scaled formation to exhibit behaviors or accomplish tasks that otherwise will be impossible to achieve with a single module [5]. Most notably, shape reconfiguration in modular robotics enables a formation of agents to deliver hybrid locomotion patterns such as walking, rolling [6], climbing [7], and undulating, or provide multiarm manipulation for high payload tasks [8].

The key enabling component of shape metamorphosis is the docking interface [9]–[11], which couples modules together in the desired formation. Typically, these interfaces are either gender [12] or genderless [13], and are developed with either magnets, electromagnets, grippers, or mechanical connectors actuated via shape memory alloys [14]. More recently, other techniques were also investigated for modular coupling, such as mechanical latching [15] and vacuum-based bonding via suction forces [10]. A summary of relevant existing interfaces and their respective robots is provided in Table I, with a more comprehensive comparison available in [16].

Although many interesting mobility and manipulation tasks have thus far been demonstrated with existing modular mobile robots [17]–[30], their ability to deliver high payload capacity and operate efficiently on a real terrain is yet to be proven. In fact, with current modular technology [1], [16], [31], a rigid-structure robot tailored to operate on a specific terrain layout is more likely to outperform its modular counterpart, despite the versatility in mobility that the latter can deliver through reconfiguration. This limitation is attributed to the docking interface, which for practical mobility and manipulation applications is required to meet the following specifications:

1) *Rigidity:* to provide coupling strength between modules and enable a scaled modular formation to behave as a rigid-structure robot.
2) *Reversibility:* to enable modules to dock and transform the shape of the formation, or undock and revert back to individual mobility.
3) *Nonback-drivability:* to prevent undesirable disconnection in the formation under excessive loading.

Developing an active coupling interface that accommodates these requirements remains a challenging objective. This is because the satisfaction of these specifications often comes at the expense of the size, the weight, and the number of actuators in the interface. These considerations are critical for modular robotics, where the objective is to maintain the simplicity of individual modules, while allowing scalability in size by coupling rudimentary modules into larger formations.

Manuscript received January 28, 2012; revised October 2, 2012 and December 25, 2012; accepted April 23, 2013. Date of publication May 21, 2013; date of current version April 11, 2014. Recommended by Technical Editor S. Verma. This work was supported by the Robotics and Mechatronics Laboratory, School of Engineering and Applied Sciences, George Washington University, Washington, DC 20052 USA.

The authors are with the Department of Mechanical and Aerospace Engineering, The George Washington University, Washington, DC 20052 USA (e-mail: paul4@gwu.edu; bentzvi@gwu.edu).

Color versions of one or more of the figures in this paper are available online at http://ieeexplore.ieee.org.

Digital Object Identifier 10.1109/TMECH.2013.2261531

To address these issues, this paper proposes a new design for active coupling that combines rigidity, reversibility, and non-back-drivability in an interface that exhibits two main attributes:

1) *A torque recirculation scheme*, which uses one central *high-torque* motor to deliver three independent modes of operation. Through a motorized sequential selection mechanism, the proposed interface can drive the module, align the active mating parts of two adjacent modules prior to docking, and create a rigid non-back-drivable joint that enables one module to rotate relative to its neighbor in a scaled formation.
2) *Compactness*, where the torque recirculation scheme reduces the number of *high-torque* motor/gearbox assemblies by two, which in turn reduces the size and weight of individual modules.

The second merit of this paper lies in the DRSR mechanism, which operates the toggling mechanism that enables the tristate operation of the proposed interface. Its value is evidenced, not only in the role it plays in initiating the tristate operation of the interface, but also in its broader industrial applications, and in its small footprint which further adds to the compactness of the interface.

In the ensuing discussion, a motivating application of the proposed coupling interface is first presented in Section II, followed by an optimal kinematic and dynamic analysis of the DRSR mechanism in Sections III and IV. This analysis is supplemented by a proof of concept prototype in Section V, which experimentally validates the interface's three modes of operation, and its rigidity relative to existing modular robots.

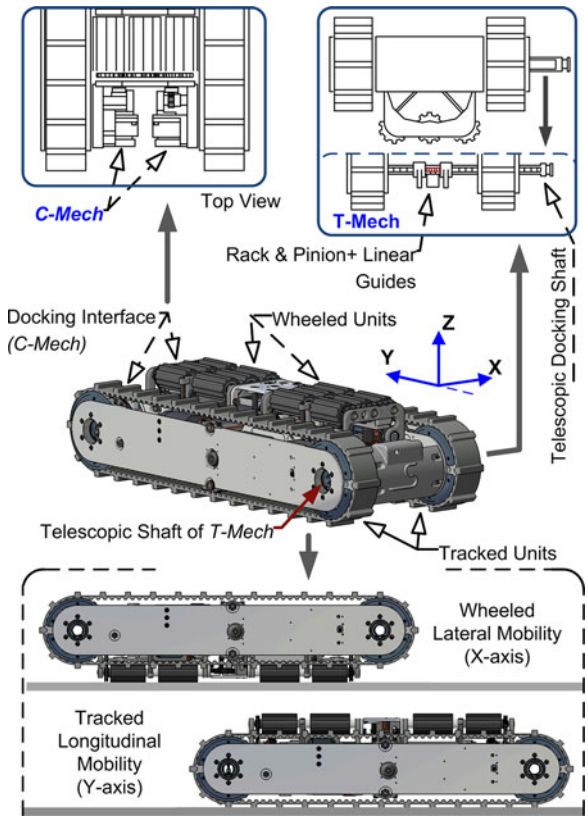


Fig. 1. Schematic of STORM's locomotion module, showing hybrid multidirectional mobility and the two components of the docking interface.

## II. Motivating Application and Overall Design

### A. STORM Modular Robot

The motivations of the proposed docking interface are attributed to reconfigurable robotic research such as STORM [32], which represents an on-going development of modular robots for high-capacity mobility and manipulation. Although the focus of this paper is on rigid non-back-drivable coupling, an overview of STORM is first presented in order to motivate the ensuing discussion with a prospective application.

STORM is comprised of two independent modules: a locomotion module shown in Fig. 1 and a manipulation module shown in Fig. 2. The locomotion module consists of a hybrid combination of wheels and tracks. These are cascaded along two orthogonal mobility axes in a way to provide bidirectional locomotion for the module. A motorized leadscrew mechanism toggles between the two mobility modes and enables the module to deliver hybrid mobility along three orthogonal axes. That is, the tracked units can be deployed to provide longitudinal mobility ($Y$-axis) with *Hilare*-type steering. Likewise, the wheeled units can be deployed via translation along the vertical prismatic axis ($Z$-axis); lifting the tracks above the ground to enable lateral mobility (with *Hilare*-type steering) as illustrated in Fig. 1. On the other hand, the manipulation module (see Fig. 2) consists of two tracked units with differential steering, and further carries a one-link arm with an end-effector which provides basic manipulation in the undocked configuration.

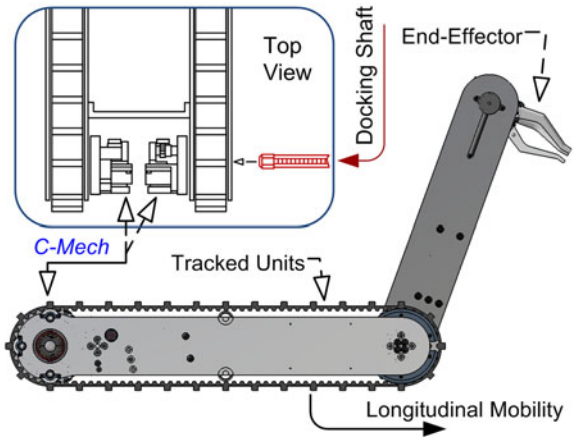


Fig. 2. CAD model of STORM's manipulation module showing the central arm and the end-effector.

Docking between different modules of STORM is enabled by the coupling interface which represents the scope of this paper. This interface is composed of a male part called the *T-Mech* (Translational Mechanism), carried by the locomotion module, and consisting of a non-back-drivable telescopic shaft that translates along the lateral direction ($X$-axis) from either side of the module. Alternatively, the female part of the coupling mechanism, called the *C-Mech*, can be carried by either the locomotion or the manipulation module, and consists of a clamping device

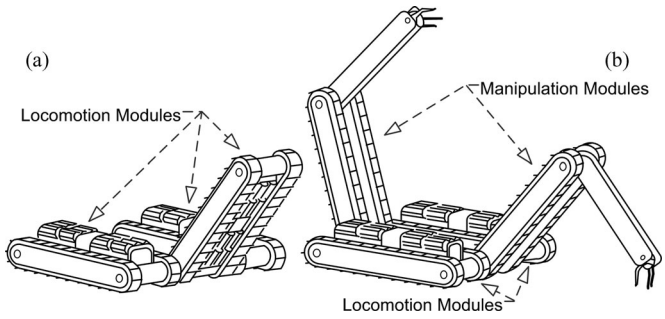


Fig. 3. Two sample STORM formations: (a) Three locomotion modules. (b) Two locomotion and two manipulation modules.

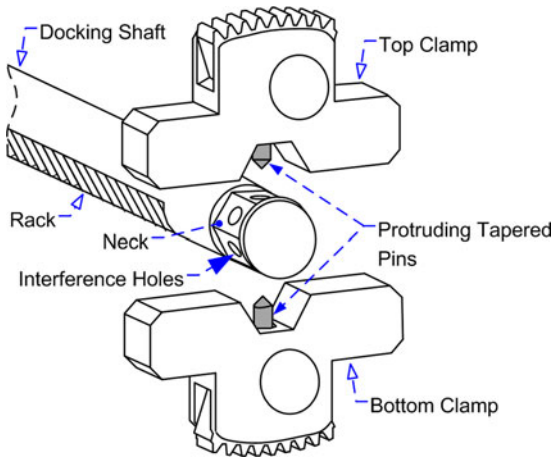


Fig. 4. Docking shaft with the hexagonal neck and the interference holes that mate with the protruded pins of the clamps

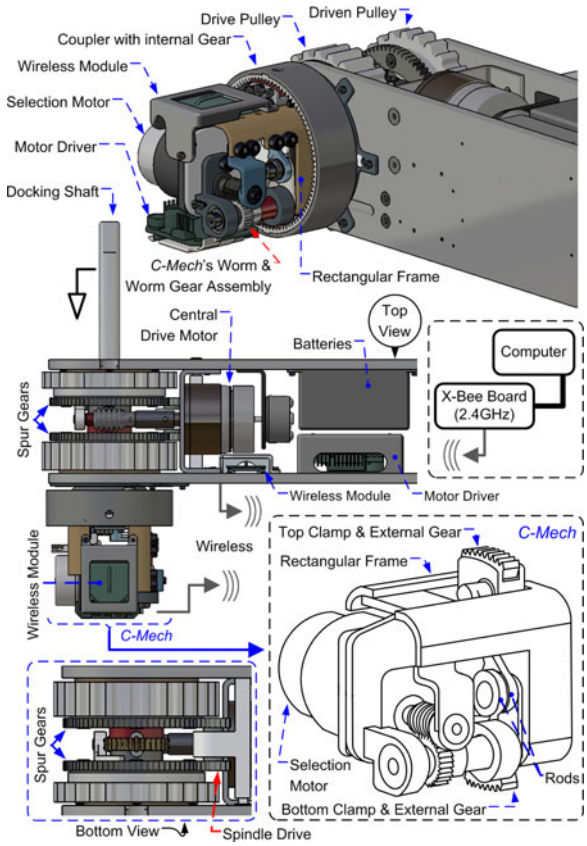


Fig. 5. CAD illustration of the proposed coupling mechanism showing all relevant mechatronic components.

and a torque recirculation scheme, both enabled by a DRSR mechanism.

Alignment between the *T-Mech*'s and the *C-Mech*'s components is provided by the multidimensional mobility of the locomotion module [32]. This enables a swarm of modules to dock into different configurations, such as the three- and four-module sample formations shown schematically in Fig. 3. The overall articulated structure of STORM was inspired by the design of the hybrid mechanism mobile robot [42]–[44].

### B. Overall Design of the Docking Interface

The coupling interface proposed in this paper satisfies the requirements of rigidity, compactness, reversibility, and non-back-drivability, and comprises two independent male (*T-Mech*) and female (*C-Mech*) components.

*1) T-Mech:* The *T-Mech* consists of a docking shaft whose linear motion is enabled by a motorized rack and pinion mechanism, where the rack is integrated in a rectangular groove inside the shaft (see Fig. 4). This translational motion is guided by two linear guides (see Fig. 1) which disable the rotation of the shaft around its centroidal axis. The docking shaft also carries two hexagonal necks—one on each end of the shaft—which mate with the combined hexagonal aperture created by the clamps of the *C-Mech* in the *clamp mode*.

Furthermore, in order to prevent the hexagonal neck from slipping inside the clamps under excessive torsional loading, two tapered pins, one carried by each clamp, create a physical interference with the mating holes of the shaft's neck (see Fig. 4). This interference significantly increases the *structural* rigidity of the interface as will be demonstrated experimentally in Section V.

*2) C-Mech:* The *C-Mech* (see Fig. 5) represents the key component that enables the interface to operate in three independent modes and consists of a motorized DRSR mechanism that translates two clamps along two parallel rails (see Fig. 6). A selection geared-motor actuates the rocker via the *C-Mech*'s worm and worm gear assembly. This assembly rotates the dual rods to initiate the clamps' translation, while ensuring the *mechanical* non-back-drivability of the mechanism in this mode.

Each clamp further carries an external gear segment (see Figs. 5 and 6) that engages the internal gear of the coupler. This coupler is rigidly connected to the driving element of the module, such as a wheel or a pulley as shown in the transmission schematic of Fig. 6(a). The rectangular frame that houses the *C-Mech* components is connected to a central hollow main shaft supported by ball bearings, while itself providing linear bearing support for the driving element of the module (wheel, pulley, etc.). This shaft carries a worm gear in the center, which transmits the torque of a central motor directly to the rectangular frame and all the elements connected to it. This direct transmission causes the *C-Mech* to rotate at the same speed as that of the main shaft at all time.

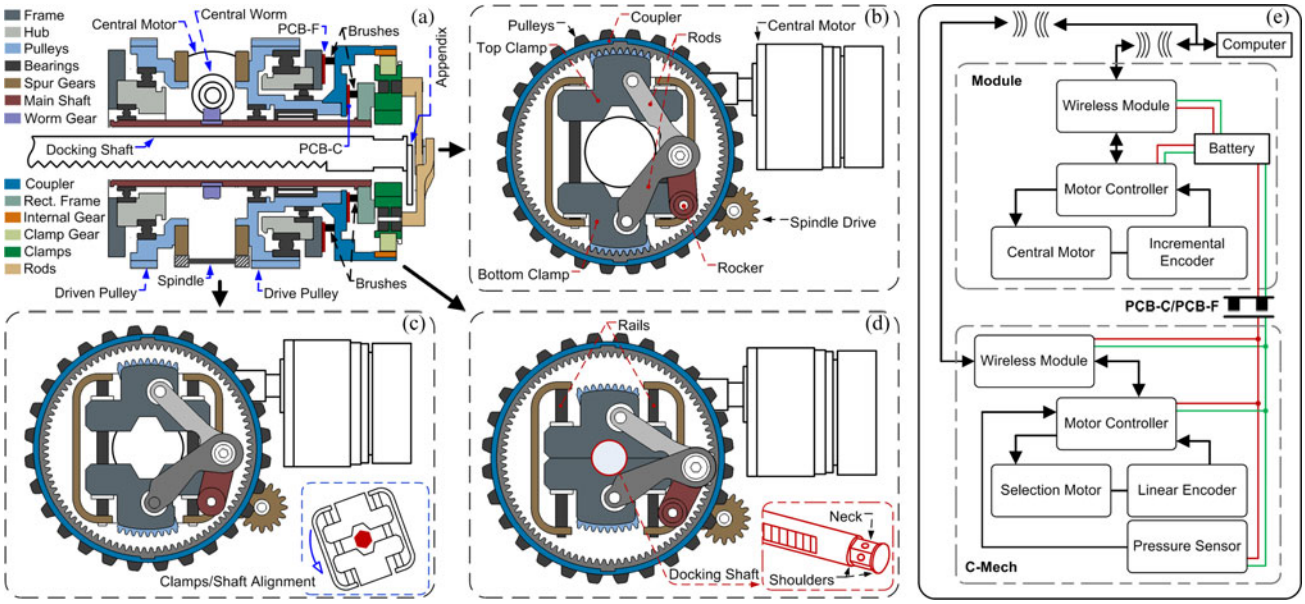


Fig. 6. (a) Simplified transmission schematic of the *C-Mech*. (b) Drive Mode. (c) Neutral mode. (d) Clamp mode. (e) Control block diagram.

The electrical components of the *C-Mech* are powered by a battery carried by the module. Power is transmitted via two pairs of graphite brushes [see Fig. 6(a)]. One pair transmits electrical current from the module to the coupler, while the other pair transmits current from the coupler to the rectangular frame, thus enabling the *C-Mech* to rotate continuously inside the coupler without being limited by wire entanglement. These electrical brushes create contact with two printed circuit boards (PCB) carrying two isolated copper rims, where one rim connects to the power terminal, and the other connects to the ground. The first PCB [see PCB-F in Fig. 6(a)] is attached to the frame of the module, while the other is attached to the internal section of the coupler [PCB-C in Fig. 6(a)].

To further support the continuous rotation of the *C-Mech* inside the coupler, sensor data and motor control commands are transmitted wirelessly between the *C-Mech* and the module. This communication protocol is based on the block diagram shown in Fig. 6(e), where a wireless network is established with two X-Bee RF receivers (2.4 GHz): one being carried by the module and the other by the *C-Mech* (see Fig. 5). Data packages shared on this network include linear encoder measurements which monitor the displacement of the two sliders, pressure sensing from the appendix [see Fig. 6(a)] which detects the end of the docking shaft's linear stroke, and position command signals to actuate the selection motor.

### C. Modes of Operation

*1) Drive Mode:* The default operation mode of the tristate docking interface is the *drive mode*, which is initiated via the DRSR by engaging the top and bottom external gears with the internal gear of the coupler as shown in Fig. 6(b). When this happens, the torque of the central motor causes the coupler to rotate at the same speed as that of the main shaft. However, since the external gear segments engage the internal gear in this mode, the motor torque will be directly transmitted to the drive pulley (or the drive wheel) through the coupler.

Furthermore, if the module is driven by tracks and pulleys, a uniform torque transmission to the tracks can be established with an offset spindle drive [see Figs. 5 and 6(a)–(b)] in the event where the motor shaft splits the pulleys in the middle (see Fig. 5). This spindle transmits the torque from the drive pulley to the driven pulley via two spur gears (see Fig. 5), where each gear is connected to each section of the pulley.

*2) Neutral Mode:* In the *neutral mode*, the clamps are positioned somewhere along the rails to disengage the internal gear as shown in Fig. 6(c). When this happens, the torque of the central motor causes the *C-Mech* to rotate idly inside the coupler. This idle rotation enables the alignment and reorientation of the clamps' semihexagonal internal apertures to the hexagonal neck of the *T-Mech*'s docking shaft prior to coupling.

*3) Clamp Mode:* In the *clamp mode*, the top and bottom clamps are driven downward along the rails until the combined hexagonal aperture of the clamps mates with the hexagonal neck of the docking shaft [see Fig. 6(d)]. This happens during docking between two adjacent modules, where the telescopic shaft of the *T-Mech* carried by the adjacent module is inserted inside the hollow interior of the main shaft until it is stopped by an appendix. This appendix is connected to the rectangular frame and further carries a pressure sensor. Its location inside the space between the clamps and the rods [best shown in Fig. 6(a)] is defined in a way to cause the vertical plane containing the two protruding pins, and that containing the interference holes, to coincide when the docking shaft is stopped by the appendix. Once this happens, the alignment between the pins and the holes will be reduced to a reorientation of the clamps about the axis of the main shaft in the *neutral mode*.

The resulting hexagonal mating is strengthened by the *mechanical* non-back-drivability of the *C-Mech*'s worm and worm

gear assembly and by the physical interference between the pins and the docking shaft. This prohibits the undesirable disengagement of the *clamp mode* by locking the clamps to the docking shaft which is held stationary by the adjacent module. Such locking prevents one module from sliding away from the other along the lateral direction ($X$-axis). It also disables the rotation of the clamps relative to the docking shaft since the two behave as a single entity in the *clamp mode*.

When this happens, the entire *C-Mech* becomes stationary relative to the docking shaft, specifically the rectangular frame which is connected to the main shaft. The stationarity of the main shaft causes the central worm gear [see Fig. 6(a)] to behave as a sun gear with respect to the worm connected to the central motor. This converts the rotation of the central motor to a revolution of the module carrying the *C-Mech* around the docking shaft which creates an active joint for this motion. In such case, the mobility of the formation (e.g., see Fig. 3(a) and (b)) will be provided by the adjacent modules since the motor torque of the middle module is redirected to rotate it around its neighbors in the *clamp mode*.

### D. Other Possible Integrations of the C-Mech

The selection of the DRSR mechanism in Fig. 6 is done for two main reasons:

1) *Compactness:* where the small projected footprint of the DRSR reduces the width of the *C-Mech*, while satisfying the rigidity, reversibility, and non-back-drivability requirements of the interface.
2) *Off-centric actuation*: where the DRSRs design-driven rocker length provides added freedom with respect to the location of the selection motor inside the coupler. This enables the containment of the entire torque recirculation scheme inside the circumference of the coupler for a wider selection of motor/gearbox assemblies.

The importance of these two advantages is put in perspective through a type synthesis process, which highlights the significance of the DRSR relative to a comparable design with a leadscrew-nut assembly as shown in Fig. 7(b). Albeit the leadscrew satisfies the non-back-drivability constraint, it in fact occupies a space that is ∼50% larger than the space occupied by the DRSR mechanism if the same motor assemblies were employed for both implementations. This extra space is required, even without the additional torque amplification stage created by the *C-Mech*'s worm and worm gear assembly [see Fig. 7(a)]. Indeed, if this second gear stage is coupled to the leadscrew, the additional space that it occupies nearly doubles the original width of the *C-Mech* implemented with a DRSR. This renders the *C-Mech* undesirably wide and subsequently impacts the width of the module.

We also highlight that in Fig. 7, the selection motor was placed in series with the leadscrew in order to contain the *C-Mech* assembly inside the coupler's circumference. Taking this requirement into consideration, Table II provides a summary of other possible embodiments of the torque recirculation scheme and a description of their most pertinent shortcomings relative to the DRSR.

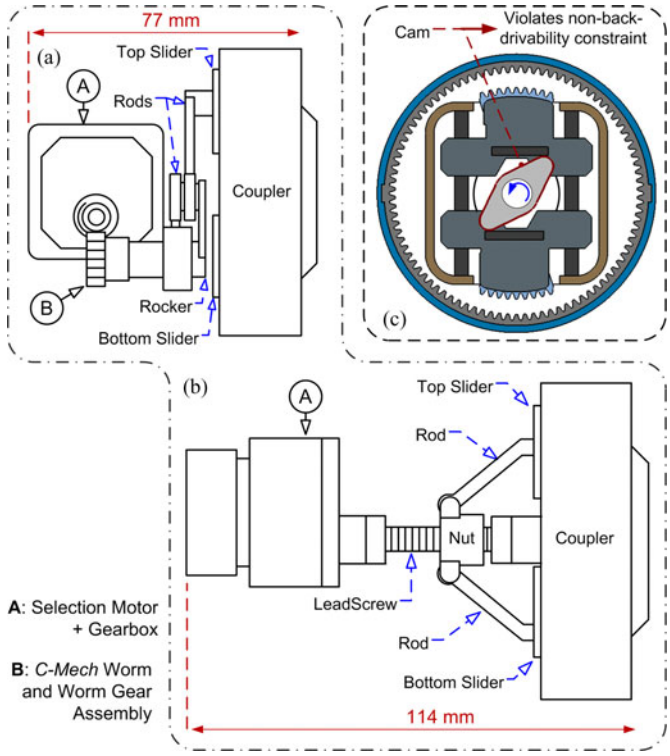


Fig. 7. Comparison of different embodiments of the *C-Mech*: (a) DRSR mechanism. (b) Leadscrew mechanism without a second torque amplification stage. (c) Cam-follower mechanism.

TABLE II
SHORTCOMINGS OF OTHER CANDIDATE EMBODIMENTS FOR THE TORQUE RECIRCULATION SCHEME

| Mechanism | Shortcomings |
|---|---|
| Cam-Follower (Fig. 7(c)) | Violates the non-back-drivability constraint due to the rolling contact between the cam and the follower |
| Twin screws Left-hand/ Right-hand Threads | Motor orientation similar to Fig. 7(b). Selection motor should be placed orthogonal to the coupler's plane to align the rotation axis of the *C-Mech*'s worm gear with the central axis of the screw. |
| Rack and Pinion | Pinions should be located along the central plane of the coupler to accommodate stroke length, therefore restricting the possibility of containing the selection/gearbox assembly inside the coupler's circumference. Opposite displacement directions of racks may dictate independent actuation of pinions. |
| Linear Actuator | Provides low push/pull force compared to the DRSR due to smaller torque amplification ratios. Implementation may dictate two actuators to drive both sliders independently |

## III. Optimal Design and Kinematic Synthesis of the DRSR

### A. Nomenclature

To study the kinematics of the DRSR mechanism, we first define a pertinent nomenclature in reference to Fig. 8.

$X_0Y_0$ Global Cartesian frame attached to the rocker joint.

$l_1, l_2, l_2'$ Length of the rocker, the top rod, and the bottom rod, respectively.

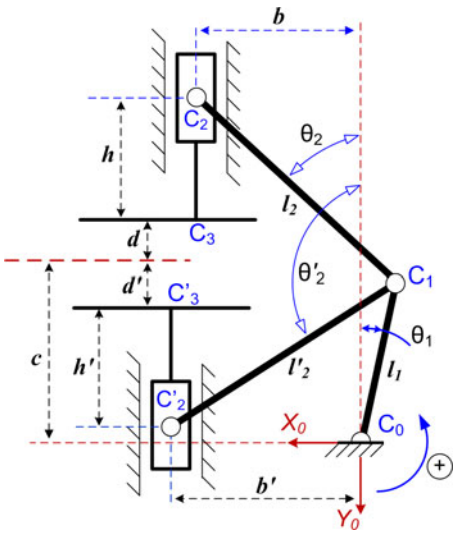


Fig. 8. Kinematic diagram of the DRSR mechanism.

| | |
|---|---|
| $\theta_1, \theta_2, \theta_2'$ | Rocker angle, top rod angle, and bottom rod angle relative to the $Y_0$-axis, respectively. |
| $b, b'$ | Distance between $Y_0$-axis and points $C_2$ and $C_2'$ along $X_0$-axis, respectively. |
| $h, h'$ | Distance $\overline{C_2C_3}$ and $\overline{C_2'C_3'}$ along $Y_0$-axis, respectively. |
| $c$ | Distance between $X_0$-axis and the central plane, measured along $Y_0$-axis. |
| $d, d'$ | Distance between the central plane and points $C_3$ and $C_3'$ measured along $\mathrm{Y}_0$-axis, respectively. |
| $d_{\max}$ | Maximum sliders' stroke along the rails, corresponding to the *drive* mode. |
| $\theta_{1,d_0}, \theta_{1,d_{\max}}$ | Rocker angle corresponding to $d = 0$ and $d = d_{\max}$, respectively. |

### B. Position Kinematics

The kinematic diagram of the DRSR mechanism is as visualized in Fig. 8. Because the motion of the rods is constrained by the sliders' translation along the rails, one can express the rods' angles in terms of the rocker angle $\theta_1$ as

$$\sin(\theta_2) = \frac{l_1 \sin(\theta_1) + b}{l_2} \tag{1}$$

$$\sin(\theta_2') = \sin(\pi - \theta_2') = \frac{l_1 \sin(\theta_1) + b'}{l_2'}. \tag{2}$$

With this, the vertical position $d$ of point $C_3$ of the top slider can be written as a function of (1) and the rocker angle $\theta_1$ in the global frame $X_0\mathrm{Y}_0$ as

$${}^0d = l_1 \cos(\theta_1) + l_2 \sqrt{1 - \left\{ \frac{l_1 \sin(\theta_1) + b}{l_2} \right\}^2} - c - h. \tag{3}$$

A similar derivation yields an expression for the vertical position $d'$ of point $C_3'$ on the bottom slider as follows:

$${}^0d' = l_1 \cos(\theta_1) - l_2' \sqrt{1 - \left\{ \frac{l_1 \sin(\theta_1) + b'}{l_2'} \right\}^2} - c + h' \tag{4}$$

where based on the orientation of the global frame defined in Fig. 8, $d > 0$ and $d' < 0$.

From (3) and (4), it is obvious that $d - |d'|$ represents an explicit function of angle $\theta_1$, and that $d - |d'| \neq 0$ even if parameters $b', l_2'$, and $h'$ were chosen equal to $b, l_2$, and $h$, respectively. This infers that the top and bottom sliders do not travel the same distance for the same rocker rotation, which prevents them from either reaching the central plane (*clamp mode*), or engaging the coupler's internal gear (*drive mode*) at the same time.

### C. Optimal Kinematic Synthesis

Because the DRSR's sliders do not travel the same distance for the same rocker rotation, an offset expression $e = d + d'$ is defined to reflect the displacement offset between the two sliders. This offset $e$ is a direct function of the rocker angle $\theta_1$ and the geometric parameters that define the DRSR, where in the most general form, one can define $e$ as

$$e = f(\theta_1, b, l_1, l_2, b', l_2', h, h', c, \theta_{1,d_0}, \theta_{1,d_{\max}}, d_{\max}). \tag{5}$$

In (5), $\theta_2, \theta_2'$ were omitted from $f$ because of direct correlation with $\theta_1$ as defined in (1) and (2). Thereafter, the objective of the kinematic synthesis is to generate optimal dimensions of the DRSR that enable the mechanism to fulfill the following specifications imposed by the interface's operation:

- C.1 Ensure that the rocker remains contained inside the coupler'scircumference at the clamp mode.
- C.2 Ensure that $e = 0$ at the clamp mode.
- C.3 Ensure that $e \simeq 0$ at the drive mode.
- C.4 Maximize the efficiency of the mechanism.
- C.5 Contain the value of $e(\theta_1)$ within a maximum allowable threshold in the intermediate stroke (neutral mode).

We note that dimensioning the DRSR mechanism to satisfy given design specifications can be broadly done using a variety of methods (trigonometric, algebraic, complex numbers method, etc.) [33]. In this analysis however, we opt for a multiobjective optimality approach [34] since it enables the formulation of a design problem with heterogeneous cost functions and constraints (geometric, kinematic, force-based, equalities and inequalities, etc.). This formulation aims at reducing the complexity of $e$ in (5), by considering the geometric and kinematic dependencies that exist between the different parameters of the DRSR in line with the imposed operation requirements of the mechanism.

First, we start the optimality analysis by assigning a choice for $(b, h)$ that maximizes the push/pull ($Y_0$-axis) component of the force transmitted to the top slider via the top rod. This is achieved by minimizing $\theta_2$ at $\theta_{1,d_0}$ since $\theta_2$ increases as $\theta_1$ decreases from $\theta_{1,d_{\max}}$ to $\theta_{1,d_0}$. Such constraint is met by placing joint $C_2$ at the intersection of the minimum value of $b$ and the maximum value of $h$ within the allowable geometric range imposed by the design dimensions of the top slider.

Furthermore, a choice for $(l_1, c, \theta_{1,d_0})$ is defined to satisfy requirement *C.1* at $\theta_1 = \theta_{1,d_0}$, irrespective of the dimensions of the bottom rod [case illustrated in the example of Fig. 6(d)]. This choice is accomplished at $\theta_1 = \theta_{1,d_0}$, i.e., $d = 0$, and is further supplemented by a choice of $d_{\max}$ that ensures the engagement of the internal gear with the external gears at the *drive mode*. Such choice depends directly on the pitch diameter of the selected internal/external gears.

These selected values of $b, h, l_1, c, \theta_{1,d_0}$, and $d_{\max}$ enable the calculation of $l_2$ as

$$l_2^2 = l_1^2 + b^2 + (c+h)^2 - 2l_1\sqrt{b^2+(c+h)^2}\cos\left(\theta_{1,d_0} + tg^{-1}\left\{\frac{b}{c+h}\right\}\right) \quad (6)$$

and the computation of $\theta_{1,d_{\max}}$ as a solution to the implicit quadratic equation

$$p\cos(\theta_{1,d_{\max}}) - b\sin(\theta_{1,d_{\max}}) = \frac{p^2 + l_1^2 - l_2^2 + b^2}{2l_1} \triangleq \rho \quad (7)$$

where $p = c + h + d_{\max}$. Equation (7) is satisfied for two solutions of $\theta_{1,d_{\max}}$ :

$$\theta_{1,d_{\max}}^{1,2} = \sin^{-1}\left(\frac{-\rho b \pm p\sqrt{p^2-\rho^2+b^2}}{b^2+p^2}\right) \quad (8)$$

which generate an *elbow-up* and an *elbow-down* configuration of the rocker and the rod. However, because the displacement of the sliders is restricted by the engagement of the internal gear with the external gear segment at the *drive mode*, the *elbow-down* solution, and the singular rocker/top-rod posture between the *elbow-up* and *elbow-down* configurations, cannot practically occur. This means that the only possible solution for (8) in this case is $\theta_{1,d_{\max}} = \theta_{1,d_{\max}}^1$.

With these established formulations, the offset expression in (5) can be reduced to $e = f(\theta_1, b', l_2', h')$. However, because such expression is a direct function of $\theta_1$, there exist no unique values for $(b', h', l_2')$ that generate a zero-offset profile ($e = 0\,\forall\theta_1$) over the entire range $\theta_{1,d_{\max}} \le \theta_1 \le \theta_{1,d_0}$.

Nonetheless, it is possible to calculate the dimensions of the lower rod/slider assembly such that the boundary conditions corresponding to the *clamp mode* $d' = 0|_{\theta_{1,d0}}$ and the *drive mode* $d' = d_{\max}|_{\theta_{1,d\max}}$ are met. This may leave the error unbounded in the *neutral mode*, which is acceptable since the sliders do not interact with any components of the docking interface when operating in this mode.

The first terminal condition considered is $d' = 0|_{\theta_{1,d0}}$ (*C.2*), since it is a more stringent design requirement to ensure that $e = 0$ at the *clamp mode*, as opposed to the *drive mode* where an $e < \varepsilon \neq 0 (\varepsilon \ll 1)$ can be tolerated. Note that minimizing $e$ at $\theta_1 = \theta_{1,d_0}$ does not necessarily yield $e = 0$. Thus, it becomes necessary to first ensure that $e = 0$ geometrically at the *clamp mode*, and then minimize $e$ to an acceptable error $\varepsilon$ at the *drive mode*. This priority is given to the *clamp mode* since the two sliders have to clamp simultaneously on the docking shaft to create a rigid revolute joint, whereas alternatively, a full engagement of only one external gear segment with the coupler's internal gear suffices to initiate the *drive mode.*

Such priority consideration allows the derivation of an expression for $l_2'$ in terms of $(b', h')$, which ensures the non-violation of this constraint $\forall\, b', h'$

$$l_2'^2 = l_1^2 + q^2 - 2ql_1\cos(\beta + \theta_{1,d_0}) \quad (9)$$

where

$$q = \sqrt{b'^2 + (c-h')^2},\ \beta = tg^{-1}\left\{\frac{b'}{c-h'}\right\}.$$

The substitution of (6) into (3) and (9) into (4) generates an offset $e$ in terms of $\theta_1, b'$, and $h'$ of the form

$$e(\theta_1, b', h') = 2l_1\cos(\theta_1) + \sqrt{l_2^2 - (l_1\sin(\theta_1) + b)^2} - \sqrt{b'^2 + (c-h')^2 + l_1^2 - \left(2\sqrt{b'^2+(c-h')^2}\right)\cdot \left(l_1\cos\left\{\theta_{1,d_0} + tg^{-1}\left(\frac{b'}{c-h'}\right)\right\}\right) - (l_1\sin(\theta_1)+b')^2} - 2c - h + h' \quad (10)$$

with the first boundary condition defined in *C.2* guaranteed through (9), (10) can be minimized at $\theta_{1,d_{\max}}$ to yield an optimal combination of $b'$ and $h'$ that can meet the second boundary condition as defined in *C.3*.

However, the cost function in (10) alone is not enough. In fact, the optimal values of $b'$ and $h'$ should, not only minimize $e$, but also maximize the push/pull ($Y_0$-axis) component of the force transmitted to the bottom slider via the bottom rod. This second objective can be achieved by defining the cost function

$$\zeta(\theta_1, b', h') = \sqrt{1 - \left(\frac{l_1\sin(\theta_1) + b'}{l_2'}\right)^2} \quad (11)$$

which denotes the efficiency (*C.4*) of the bottom slider mechanism as the ratio $\zeta(\%) = \left({}^0F_{C_1C_2'}\right)_{Y_0} \Big/ {}^0F_{C_1C_2'}$, where ${}^0F_{C_1C_2'}$ defines the force transmitted by the bottom rod along its line of action and expressed in the global frame, and $\left({}^0F_{C_1C_2'}\right)_{Y_0}$ the component of ${}^0F_{C_1C_2'}$ along the $Y_0$-axis.

On the other hand, because the offset $e$ is left unbounded between the boundary conditions, it becomes necessary to cap the supremum of the set $e(\theta_1, b', h')$ to an acceptable threshold $\delta$ in the neutral zone in line with the design requirement *C.5*. This truncation, along with the geometric constraints imposed on $b'$ and $h'$, generates a multiobjective optimization problem which can be resolved at the remaining boundary $d' = d_{\max}|_{\theta_{1,d\max}}$ to yield an optimal pair $(b', h')$. The resulting optimality problem can be stated as follows:

$$\underset{b',h'\in\Omega}{\text{Min}} \quad e(\theta_1, b', h')|_{\theta_{1,d\max}}$$

$$\underset{b',h'\in\Omega}{\text{Max}} \quad \zeta(\theta_1, b', h')|_{\theta_{1,d\max}}$$

$$\text{subject to} \quad \sup|e(\theta_1, b', h')| < \delta$$

$$\text{and the set of geometric constraints } \Omega = \begin{cases} b'_{\min} \le b' \le b'_{\max} \\ h'_{\min} \le h' \le h'_{\max} \end{cases} \quad (12)$$

where $b'_{\min}, b'_{\max}, h'_{\min}, h'_{\max}$ define the bounds of the allowable range of values of $b'$ and $h'$, respectively. This range is dictated by the desirable design size of the sliders.

We note that, in (12), the value of the efficiency cost function $\zeta(\theta_1, b', h')$ is indeed most critical at the *clamp mode* ($\theta_1 = \theta_{1,d_0}$), where the angle between the bottom rod and the central plane $(\theta_2' - \pi/2)$ reaches its minimum value corresponding to the least efficiency. However, since the maximization of $\zeta$ has the effect of placing joint $C_2'$ at the closest possible to the $Y_0$-axis, and at the farthest possible from point $C_3'$ along $X_0$-axis,

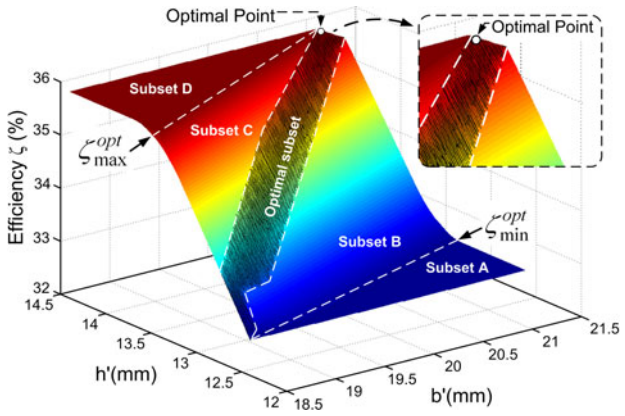


Fig. 9. Meshed solution space of the optimization problem defined in (13).

maximizing $\zeta$ at either the *drive mode* or the *clamp mode* has a similar effect with respect to the optimal location of joint $C_2'$ on the bottom slider. Indeed, such location will also take into consideration the optimal value of $e$ as dictated by (12).

### D. Optimal Solution: A Case Study

To visualize the solution of the optimal problem in (12), a case-study design for the docking interface is proposed based on the details illustrated in Fig. 5. For this case study, the length of the rocker is selected at $l_1 = 17.7\,\mathrm{mm}$, and its pivot axis is positioned at $c = 19\,\mathrm{mm}, b = 18.1\,\mathrm{mm}$ with $\theta_{1,d_0} = 27^\circ$. This combination ensures that the rocker remains contained inside the coupler at $d = d' = 0$.

Furthermore, the pitch diameter of the selected internal gear ($\phi_{\mathrm{PD}} = 75\,\mathrm{mm}$) and the height of the sliders dictate a maximum stroke length $d_{\max} = 11\,\mathrm{mm}$, with the minimum value of $h$ that the dimensions of the sliders tolerate being $h = 14.1\,\mathrm{mm}$. This yields $\theta_{1,d_{\max}} = -4.05^\circ$ and $l_2 = 31.35\,\mathrm{mm}$.

Thus, for a range of $18.5\,\mathrm{mm} \le b' \le 26.5\,\mathrm{mm}$ and $10.5\,\mathrm{mm} \le h' \le 14.4\,\mathrm{mm}$ dictated by the dimensions of the bottom slider, the multiobjective optimization problem in (12) can be solved iteratively if one converts the offset cost function into an inequality constraint. That is, since it is a design requirement to ensure that $e \simeq 0$ at $\theta_1 = \theta_{1,d_{\max}}$ (*C.3*), the problem in (12) can be restated as a suboptimal formulation as

$$\underset{b',h' \in \Omega}{\mathrm{Max}} \quad \zeta(\theta_1, b', h')|_{\theta_{1,d_{\max}}}$$

$$\text{subject to} \quad g(\theta_1, b', h') = \begin{cases} |e(\theta_1, b', h')|)_{\theta_{1,d_{\max}}} < \varepsilon \\ \sup |e(\theta_1, b', h')| < \delta \end{cases}$$

and the set of geometric constraints

$$\Omega = \begin{cases} 18.5 \le b' \le 26.5 \\ 10.5 \le h' \le 14.4 \end{cases} \tag{13}$$

where $\varepsilon \ll 1$ and $\delta < 0.6\,\mathrm{mm}$ for this case study. The choice of $\delta$ is generally a design compromise between an acceptable maximum offset $e$, and an acceptable minimum efficiency $\xi$. We note that thereafter, the term "optimal" and "suboptimal" will be used interchangeably.

A candidate solution of (13) is visualized in Fig. 9 as part of a meshed space $\mathbb{S} \subset \Lambda$ ($\Lambda$ is the meshed space of $\Omega$). This space is divided into five subsets of pairs $(b', h')$ defined as follows.

1) Subset $A \subset \mathbb{S}$ contains the pairs $(b', h')$ which violate $g(\theta_1, b', h')$ and generate an efficiency $\zeta_A < \min(\zeta_{\mathrm{Optimal\,Subset}}) \triangleq \zeta_{\min}^{\mathrm{opt}}$. This subset is thus capped at the value corresponding to $\zeta_{\min}^{\mathrm{opt}}$.
2) Subset $B \subset \mathbb{S}$ contains the pairs $(b', h')$ which meet *at best* one constraint of $g(\theta_1, b', h')$ but generate an efficiency comparable to that of the optimal subset.
3) The optimal subset encompasses the pairs $(b', h')$ which meet both constraints in $g(\theta_1, b', h')$, and thus contains the optimal pair $(b', h')^{\mathrm{opt}}$ . Note that the boundaries delineating the ensemble of optimal pairs $(b', h')$ are inclusive of the optimal subset.
4) Subset $C \subset \mathbb{S}$ contains the pairs $(b', h')$ which violate $g(\theta_1, b', h')$ but generate an efficiency comparable to that of the optimal subset.
5) Subset $D \subset \mathbb{S}$ contains the pairs $(b', h')$ which violate $g(\theta_1, b', h')$ but generate an efficiency $\zeta_D > \max(\zeta_{\mathrm{Optimal\,Subset}}) \triangleq \zeta_{\max}^{\mathrm{opt}}$. This subset is capped at the value corresponding to $\zeta_{\max}^{\mathrm{opt}}$.

Fig. 9 further visualizes the variation of the efficiency $\zeta$ as a function of the design parameters. Based on this illustration, one can select the optimal pair $(b', h')^{\mathrm{opt}}$ that maximizes the efficiency and minimizes the offset at the upper bound of the optimal set corresponding to $b' = 21.02\,\mathrm{mm}, h' = 14.39\,\mathrm{mm}$, and $\zeta = 35.5\%$ for this case-study.

## IV. Dynamic Simulation

A case-study dynamic simulation is conducted to validate the optimality analysis of the DRSR mechanism presented in Section III. That is, for a given torque or velocity input to the rocker, the objective is to prove that the optimal pair $(b', h')^{\mathrm{opt}}$ enables the sliders to simultaneously meet the boundary conditions corresponding to the *clamp mode* and the *drive mode*, while truncating the maximum displacement offset to the threshold $\delta$ in the *neutral mode*.

The equations of motion resulting from a Newtonian dynamic balance of forces and moments acting on the DRSR's links generate a system of 23 equations with 23 unknowns. These can be arranged in a matrix form [35] as

$$[\mathbf{C_F}(\theta)]^{23\times 12}\,{}^0F_{\mathrm{ext}} + [\mathbf{D}_\tau]^{23\times 1}\,{}^0\tau_{\mathrm{ext}} + [\mathbf{V}(\theta)]^{23\times 2}\,{}^0\dot{\theta} - [\mathbf{M}]^{23\times 8}\,{}^0a_G = \left[C_{\boldsymbol{\omega}}(\theta, \dot{\theta})\right]^{23\times 1} \tag{14}$$

with ${}^0\dot{\theta} = \left[{}^0\dot{\theta}_2\ {}^0\dot{\theta}_2'\right]^T$ and ${}^0F_{\mathrm{ext}}, {}^0\tau_{\mathrm{ext}}$ the vectors of external forces and moments acting on the links of the DRSR, respectively. In (14), $\mathbf{C_F}(\theta)$ and $\mathbf{D}_\tau$ are the matrix coefficients of external forces and torques, respectively. $\mathbf{V}(\theta)$ is the matrix coefficient of angular velocities of the top and bottom rods, $\mathbf{M}$ is the mass matrix, ${}^0a_G$ the acceleration vector components of the links' center of masses, and $C_{\boldsymbol{\omega}}(\theta, \dot{\theta})$ the input vector, most notably, the applied rocker angular velocity.

For this case-study, the rocker is set to rotate at a constant angular speed $\dot{\theta}_1 = 30^\circ/\mathrm{s}$. A coefficient of static friction $\mu_s = 0.3$ is applied to the sliding motion along the rails and the

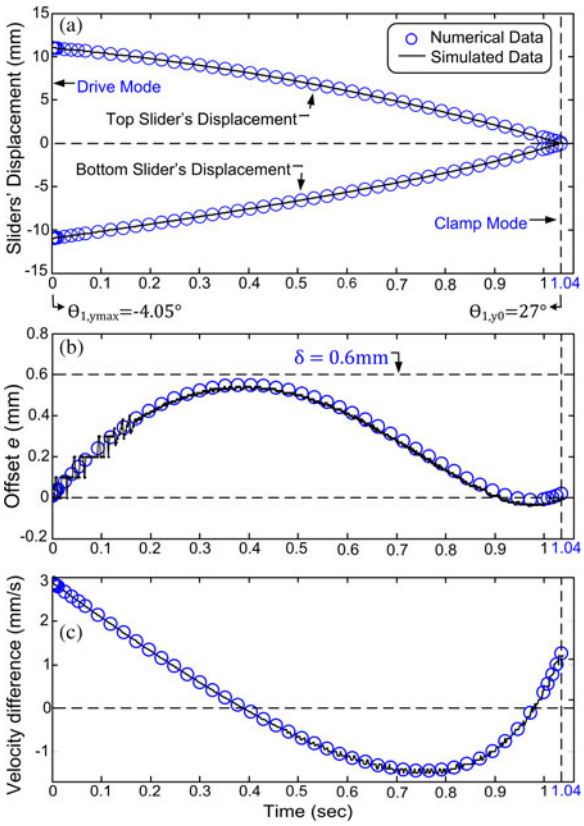


Fig. 10. Comparison between numerical solution of (14) and MSC Adams DRSR simulation for (a) Displacement of top and bottom sliders. (b) Displacement offset $e$. (c) Velocity difference between the top and bottom sliders, all plotted for a rocker angular velocity $\dot{\theta}_1 = 30°/\text{s}$.

scenario where the DRSR is driven down from the *drive* to the *clamp* mode is simulated. A numerical solution of (14) is first derived and the results are cross-compared with a dynamic simulation carried on *MSC Adams* [36]. The results from both solutions are plotted in Fig. 10.

In Fig. 10(a), the displacement of the top and bottom sliders is plotted as a function of time, where the time required by both sliders to cover their full-length stroke is 1.04 s. More importantly, both sliders start from the same position corresponding to the *drive mode*, and reach the *clamp mode* simultaneously, despite the displacement [see Fig. 10(b)] and velocity [see Fig. 10(c)] offset that exists between the two sliders.

Moreover, Fig. 10 proves that the offset profile in the *neutral zone* remains bounded, with a maximum offset $e_{\max} < \delta = 0.6\,\text{mm}$. This complies with the required operation of the interface, and further validates the optimality analysis of the DRSR mechanism presented in Section III.

## V. Proof of Concept Model of the Tristate Docking Interface and the DRSR

### A. Experimental Physical Model Integration

A proof-of-concept physical model was developed to demonstrate the three modes of operation of the tristate docking interface and to measure the clamping strength of the active joint in the *clamp mode*. This model is also used to experimentally validate the kinematic properties of the DRSR mechanism, and its ability to satisfy the terminal boundary conditions corresponding to the ascending and descending strokes, derived in the optimality analysis in Sections III and IV.

The model shown in Figs. 11 and 12 consists of the docking mechanism, coupled to the transmission of a small mobile robot with a spherical wheel at the opposite end of the pulleys. A brushless dc motor (Maxon Flat, 22 V, 0.5 A) was used to drive the linkage mechanism with a peak power of 15 W, and was coupled directly to a spur gearbox with a 30:1 ratio. A second gear stage was accomplished via the *C-Mech*'s worm and worm gear assembly with an extra 30:1 ratio. This gear train delivers a peak torque of 12.5 N·m at an angular speed of 20 °/s. With this motor selection, the total weight of the first-generation *C-Mech* shown in Fig. 11 was 425 g.

Similarly, the central brushless dc motor (Maxon Flat, 22 V, 3.5 A) selected for this model delivers a peak power of 50 W, and is also coupled to a spur gearbox (26:1 ratio) and to a central worm and worm gear assembly (30:1 ratio). This gear train delivers a peak torque of 35 N·m at a nominal angular speed of 40 °/s.

A 10-bit incremental encoder (US-Digital, 1024 CPR, 5 V TTL) was connected to a customized shaft protruding from the back-end of the central motor (see Fig. 11) which interfaces with its controller (all motion, EZSV-23, 5 A max, 22 V) housed inside the module. On the other hand, a high-resolution (5 $\mu$m/count) linear encoder (Mercury, 1520P-L30 series, 5 V TTL), with the head attached to one slider and the scale to the other slider, was also integrated in the *C-Mech*. This encoder measures the sliders' total displacement, which is fed to the controller of the selection motor (EZSV-17, 2 A max, 22 V) to control the clamps' position along the rails. This sensing scheme also includes a pressure sensor (variable resistor 100 KΩ–1 MΩ), which detects the docking shaft upon contact with the appendix. Data between the motor controllers and an operating computer are circulated over the established local X-Bee network (ISM 2.4 GHz, 3.5 V, 0.2 A), as shown in Fig. 11.

### B. Experimentations and Strength Quantification

With this proof-of-concept model, the three modes of operation of the proposed interface were tested as shown in Fig. 12 and in the video file in [37]. This includes the *drive*, *neutral,* and *clamp* modes, where in the latter, the docking shaft was held stationary, and the central motor was actuated to revolve the robot around this joint (robot weight = 2.5 Kg, required peak torque for rotation about active joint ∼4 N·m).

More importantly, this model was used to quantify the strength of the active joint in the *clamp mode*, measured with a digital torque wrench connected to the tip end of the docking shaft (*Dia* = 13 mm). Hereafter, we define the interface's strength as the maximum torque capacity of the active docking joint. Because of the physical interference created between the protruded pins and the neck holes, the strength of the proposed interface is in fact independent of the clamping force applied by the rods onto the clamps once the interference is initiated. This property is highlighted through a finite element analysis of the docking shaft and the *C-Mech* assembly in the *clamp mode*.

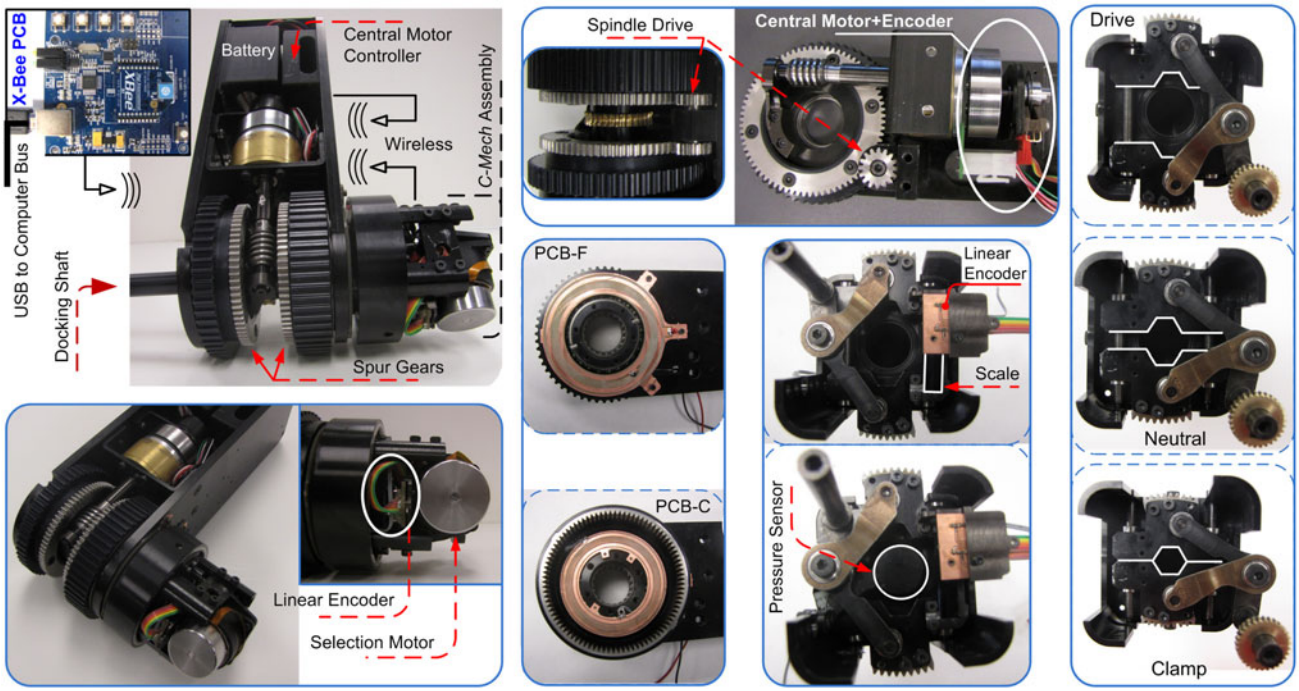


Fig. 11. Experimental physical model of the docking interface showing the *C-Mech* connected to the transmission of a small mobile robot, the DRSR in the three modes, the sensing elements of the *C-Mech*, and the two PCB's that transmit battery power (22 V) from the module to the *C-Mech*.

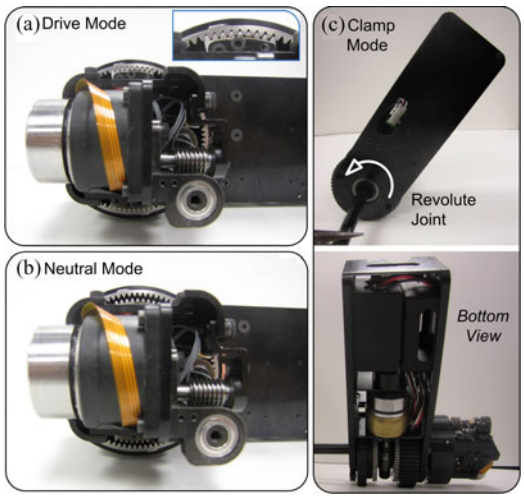


Fig. 12. Three operation modes of the docking interface. (a) Drive mode. (b) Neutral mode. (c) Clamp mode showing the revolute motion of the robot around the active joint created by the docking shaft.

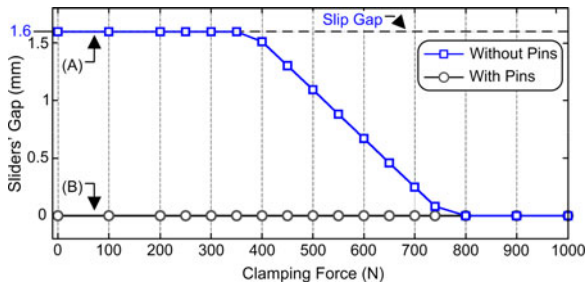


Fig. 13. FEA comparison of required clamping force for an input joint torque of 10 N·m. (a) Clamps without pins. (b) Clamps with pins.

TABLE III
INTERFACE STRENGTH FOR TWO DIFFERENT EMBODIMENTS OF THE PINS

| Pin Diameter | Pin Material | Interference Depth/Pin | Shaft Material | Max. Joint Torque |
|---|---|---|---|---|
| 2.3 mm | Steel | 3.5 – 4 mm | Aluminum | 22 N·m |
| 3.2 mm | Steel | 3.5 – 4 mm | Aluminum | 42.5 N·m |

The results of this analysis are plotted in Fig. 13 for a sample constant joint torque of 10 N·m. In this figure, the sliders' gap defines the distance $\overline{C_3C_3'}$ (see Fig. 8), and the slip gap defines the maximum value of $\overline{C_3C_3'}$ before the docking shaft's hexagonal neck slips completely inside the clamps' mating aperture. For the docking shaft of the developed model (Neck's diameter = 12 mm), the slip gap is 1.6 mm.

Through this comparison, it is shown that, while ~800 N of clamping force is required to secure a rigid clamping ($\overline{C_3C_3'} \simeq 0$) on the docking shaft for an input joint torque of 10 N·m, such force is reduced to practically zero in the presence of pins. This is because the interference created by the pins causes the two clamps to twist as a rigid body instead of separating, making the sliders' gap an independent function of the clamping force. Such structural behavior propagates the joint load toward the rails rather than causing a separation.

As a result, the rigidity of the interface is increased significantly, where the clamping strength becomes a direct function of the structural properties of the interface, and can be amplified by modifying the dimensions of the *C-Mech*, such as increasing the pins diameter. This is depicted in two sample experiments carried on the proof-of-concept prototype shown in Fig. 11 and summarized in Table III.

The significance of this rigidity is further highlighted through a comparison between the measured strength of the interface

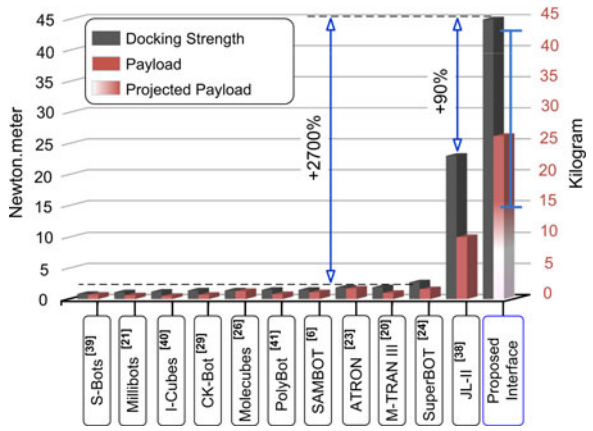


Fig. 14. Docking strength and corresponding payload comparison between the proposed mechanism and existing interfaces for a selection of modular robots.

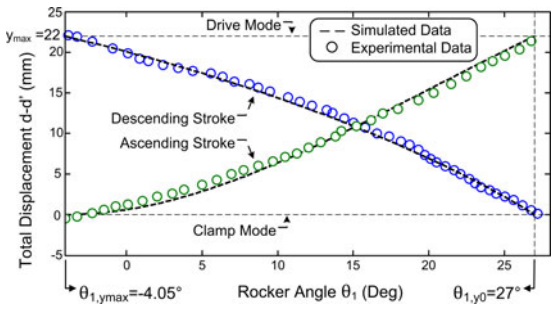


Fig. 15. Total displacement of the top and bottom sliders measured as a function of the rocker angle for the ascending and descending strokes.

and the strength of a selection of existing modular robots as illustrated in Fig. 14. In this comparison, it is noted that the strength of the proposed interface is ∼2700% higher than the average strength of most existing modular mobile robots, and ∼90% higher than the highest strength for a modular mobile robot (JL-II [38]) as reported in the literature.

Therefore, by statistically extrapolating the relationship between docking strength and payload capacity in Fig. 14, one can expect a payload of ∼26.2 Kg with the proposed interface, with a statistical low of 18.5 Kg and a high of 41.8 Kg. This represents an increase of ∼160% in capacity compared to the highest existing payload for a mobile modular robot.

### C. Measurement Validation of the DRSR Optimal Kinematics

The proof-of-concept model of the docking interface is further employed to validate the DRSR's kinematic characteristics resulting from the optimality analysis in Sections III and IV. Using the integrated linear encoder (see Fig. 11), the total displacement of the DRSR's sliders is measured as a function of the rocker angle $\theta_{1,d_{\max}} \leq \theta_1 \leq \theta_{1,d_0}$, which was measured by an external 9-bit incremental encoder (512 CPR) on a temporary experimental setup. These measurements are plotted in Fig. 15 for both the ascending (from *clamp* to *drive*) and descending strokes (from *drive* to *clamp*).

In both cases, the measured data is cross-compared with the sum of the simulated displacement data for both sliders, shown earlier in Fig. 10(a). This comparison proves the feasibility of the optimality analysis at, and between the terminal boundaries of the *clamp* and *drive modes*, where the simulated data closely matches the measurements within a ∼0% offset at the boundaries, and an average percent offset of ∼±1.5% (peak ∼ ±4.6%) in the *neutral mode*. This offset is attributed to intrinsic manufacturing tolerances, bearing misalignments, etc.

## VI. Conclusion and Future Work

This paper presented the analysis, design, and implementation of a new rigid, reversible, and non-back-drivable docking interface for modular robotic applications. The first merit of this interface lies in its rigidity, compactness, and ability to recirculate motor torque to deliver three operation modes using a single *high-torque* motor. The second merit stems from the discussion and synthesis of a new mechanism, the DRSR, which toggles between the interface's three operation modes. We believe that the DRSR, along with the torque recirculation scheme, hold a valuable industrial and research merit for applications where weight and size are a critical design constraint, such as in mobile robotics and space applications.

The methods described in this paper are part of a larger research effort to investigate modular robotics for rough terrain mobility and manipulation, and we will be exploring the integration and autonomy of the proposed mechanisms on STORM's modules in the future.

## Acknowledgment

The authors thank Z. Ma for his contributions to the integration of the prototype.

## References

[1] M. Yim, W.-M. Shen, B. Salemi, D. Rus, M. Moll, H. Lipson, E. Klavins, and G. S. Chirikjian, "Modular self-reconfigurable robot systems: Challenges and opportunities for the future," *IEEE Robot. Autom. Mag.*, vol. 14, no. 1, pp. 2–11, Mar. 2007.

[2] T. Fukuda and Y. Kawauchi, "Method of autonomous approach, docking and detaching between cells for dynamically reconfigurable robotic system CEBOT," *Int. J. Jpn. Soc. Mech. Eng.*, vol. 33, no. 2, pp. 263–268, 1990.

[3] K. Roufas, Y. Zhang, D. Duff, and M. Yim, "Six degree of freedom sensing for docking using IR LED emitters and receivers," presented at the 7th Int. Symp. Exp. Robot., Honolulu, HI, USA, 2000.

[4] C. Bererton and P. Khosla, "Toward a team of robots with repair capabilities: A visual docking system," in *Proc. 7th Int. Symp. Exp. Robot.*, 2000, pp. 333–342.

[5] G. Zhang, G. Fricke, and D. Garg, "Spill detection and perimeter surveillance via distributed swarming agents," *IEEE/ASME Trans. Mechatronics*, vol. 18, no. 1, pp. 121–129, Feb. 2013.

[6] H. Wei, Y. Chen, J. Tan, and T. Wang, "Sambot: A self-assembly modular robot system," *IEEE/ASME Trans. Mechatronics*, vol. 16, no. 4, pp. 745–757, Aug. 2011.

[7] T. W. Seo and M. Sitti, "Tank-like module-based climbing robot using passive compliant joints," *IEEE/ASME Trans. Mechatronics*, vol. 18, no. 1, pp. 397–408, Feb. 2013.

[8] S. Nouyan, R. Groß, M. Dorigo, M. Bonani, and F. Mondad, "Group transport along a robot chain in a self-organized robot colony," in *Proc. 9th Int. Conf. Intell. Auton. Syst.*, Japan, 2006, pp. 433–442.

[9] M. Nilsson, "Essential properties of connectors for self-reconfiguring modular robots," in *Proc. Workshop Reconfig. Robots, IEEE Int. Conf. Robot. Autom.*, Seoul, Korea, May 2001.

[10] R. F. M. Garcia, J. D. Hiller, K. Stoy, and H. Lipson, "A vacuum-based bonding mechanism for modular robotics," *IEEE Trans. Robot.*, vol. 27, no. 5, pp. 876–890, Oct. 2011.

[11] B. Khoshnevis, P. Will, and W. Shen, "Highly compliant and self-tightening docking modules for precise and fast connection of

self-reconfigurable robots," in *Proc. IEEE Int. Conf. Robot. Autom.*, 2003, Taipei, Taiwan, pp. 2311–2316.
[12] M. Delrobaei and K. A. McIsaas, "Connection mechanism for autonomous self-assembly in mobile robots," *IEEE Trans. Robot.*, vol. 25, no. 6, pp. 1413–1419, Dec. 2009.
[13] W-M. Shen, R. Kovac, and M. Rubenstein, "SINGO: A single-end-operative and genderless connector for self-reconfiguration, self-assembly and self-healing," in *Proc. IEEE Int. Conf. Robot. Autom.*, 2009, pp. 4253–4258.
[14] S. Murata, E. Yoshida, H. Kurokawa, K. Tomita, and S. Kokaji, "Self-repairing mechanical systems," *J. Auton. Robots*, vol. 10, pp. 7–21, 2001.
[15] A. Sproewitz, M. Asadpour, Y. Bourquin, and A. J. Ijspeert, "An active connection mechanism for modular self-reconfigurable robotic systems based on physical latching," in *Proc. IEEE Int. Conf. Robot. Autom.*, Pasadena, CA, USA, 2008, pp. 3508–3513.
[16] P. M. Moubarak and P. Ben-Tzvi, "Modular and reconfigurable mobile robotics," *J. Robot. Auton. Syst.*, vol. 60, no. 12, pp. 1648–1663, Dec. 2012.
[17] M. Yim, Y. Zhang, K. Roufas, D. Duff, and C. Eldershaw, "Connecting and disconnecting for chain self-reconfiguration with polybot," *IEEE/ASME Trans. Mechatronics*, vol. 7, no. 4, pp. 442–451, Dec. 2002.
[18] D. Rus and M. Vona, "Crystalline robots: Self-reconfiguration with compressible unit modules," *J. Auton. Robots*, vol. 10, no. 1, pp. 107–124, 2002.
[19] C. Ünsal, H. Kiliççöte, and P. K. Khosla, "A 3-D modular self-reconfigurable bipartite robotic system: Implementation and motion planning," *J. Auton. Robots*, vol. 10, no. 1, pp. 23–40, 2001.
[20] S. Murata, E. Yoshida, A. Kamimura, H. Kurokawa, K. Tomita, and S. Kokaji, "M-TRAN: Self-reconfigurable modular robotic system," *IEEE/ASME Trans. Mechatronics*, vol. 7, no. 4, pp. 431–441, Dec. 2002.
[21] H. B. Brown, J. M. Vande Weghe, C. A. Bererton, and P. K. Khosla, "Millibot train for enhanced mobility," *IEEE/ASME Trans. Mechatronics*, vol. 7, no. 4, pp. 452–461, Dec. 2002.
[22] K. Motomura, A. Kawakami, and S. Hirose, "Development of arm equipped single wheel rover: effective arm-posture-based steering method," in *Proc. IEEE Int. Conf. Robot. Autom.*, 2003, Nevada, USA, pp. 63–68.
[23] E. H. Østergaard and K. Kassow, "Design of the ATRON lattice-based self-reconfigurable robot," *J. Auton. Robots*, vol. 21, no. 2, pp. 165–183, 2006.
[24] B. Salemi, M. Moll, and W-M. Shen, "SUPERBOT: A deployable, multi-functional, and modular self-reconfigurable robotic system," in *Proc. IEEE/RSJ Int. Conf. Intell. Robots Syst.*, 2006, Beijing, China, pp. 3636–3641.
[25] S. C. Goldstein, J. D. Campbell, and T. C. Mowry, "Programmable matter," *IEEE Comput.*, vol. 38, no. 6, pp. 99–101, May 2005.
[26] V. Zykov, E. Mytilinaois, M. Desnoyer, and H. Lipson, "Evolved and designed self-reproducing modular robotics," *IEEE Trans. Robot.*, vol. 23, no. 2, pp. 308–319, Apr. 2007.
[27] V. Trianni, S. Nolfi, and M. Dorigo, "Cooperative hole avoidance in a swarm-bot," *J. Robot. Auton. Syst.*, vol. 54, no. 2, pp. 97–103, 2006.
[28] J. Liu, S. Ma, Y. Wang, and B. Li, "Network-based reconfiguration routes for a self-reconfigurable robot," *J. Sci. China, Inf. Sci.*, vol. 51, no. 10, pp. 1532–1546, Aug. 2008.
[29] M. Park, S. Chitta, A. Teichman, and M. Yim, "Automatic configuration recognition methods in modular robots," *Int. J. Robot. Res.*, vol. 27, no. 3–4, pp. 403–421, Mar. 2008.
[30] G. Ryland and H. H. Cheng, "Design of iMobot, an intelligent reconfigurable mobile robot with novel locomotion," in *Proc. IEEE Int. Conf. Robot. Autom.*, AK, USA, 2010, pp. 60–65.
[31] K. Gilpin and D. Rus, "Modular robot systems: From self-assembly to self-disassembly," *IEEE Robot. Autom. Mag.*, vol. 17, no. 3, pp. 38–55, 2010.
[32] P. Moubarak and P. Ben-Tzvi. (2011, Feb.). *STORM Animation* [Online]. Available: http://www.seas.gwu.edu/bentzvi/STORM/STORM_VR_Animation.html
[33] L. G. Reifschnider, "Teaching kinematic synthesis of linkages without complex mathematics," *J. Ind. Technol.*, vol. 21, no. 4, Oct. 2005.
[34] Y.-P. Yang, J.-J. Liu, D.-H. Ye, Y.-R. Chen, and P.-H. Lu, "Multiobjective optimal design and soft landing control of an electromagnetic valve actuator for a camless engine," *IEEE/ASME Trans. Mechatronics*, vol. 18, no. 3, pp. 963–972, Jun. 2013.
[35] M. Liu, Y. Cao, Q. Zhang, and H. Zhou, "Kinematics and dynamics simulation of the slider-crank mechanism based on MATLAB/simulink," in *Proc. Int. Conf. Comput. Appl. Syst. Model.*, China, pp. 557–563.
[36] MSC ADAMS Dynamics. (2011, Dec.). [Online]. Available: http://www.mscsoftware.com/products/cae-tools/adams.aspx
[37] P. Moubarak, P. Ben-Tzvi, and Z. Ma. (2012, Jan.). *Demonstration of the three modes of operation of the tri-partite docking interface* [Online]. Available: www.seas.gwu.edu/bentzvi/STORM/DOK2.html
[38] W. Wang, W. Yu, and H. Zhang, "JL-2: A mobile multi-robot system with docking and manipulating capabilities," *Int. J. Adv. Robot. Syst.*, vol. 7, no. 1, pp. 009–018, Feb. 2010.
[39] R. Gro$\beta$, M. Bonani, F. Mondada, and M. Dorigo, "Autonomous self-assembly in swarm-bots," *IEEE Trans. Robot.*, vol. 22, no. 6, pp. 1115–1130, Dec. 2006.
[40] C. Ünsal and P. K. Khosla, "A multi-layered planner for self-reconfiguration of a uniform group of I-cube modules," in *Proc. IEEE/RSJ Int. Conf. Intell. Robots Syst.*, 2001, Hawaii, USA, pp. 598–605.
[41] D. G. Duff, M. H. Yim, and K. D. Roufas, "Evolution of PolyBot: A modular reconfigurable robot," presented at the Harmon. Drive Int. Symp., Nagano, Japan, 2001.
[42] P. Ben-Tzvi, "Experimental validation and field performance metrics of a hybrid mobile robot mechanism," *J. Field Robot.*, vol. 27, no. 3, pp. 250–267, May 2010.
[43] P. Ben-Tzvi, A. A. Goldenberg, and J. W. Zu, "Design and analysis of a hybrid mobile robot mechanism with compounded locomotion and manipulation capability," *J. Mech. Design,*, vol. 130, no. 7, pp. 1–13, Jul. 2008.
[44] P. Ben-Tzvi, A. A. Goldenberg, and J. W. Zu, "Articulated hybrid mobile robot mechanism with compounded mobility and manipulation and on-board wireless sensor/actuator control interfaces," *Mechatron. J.*, vol. 20, no. 6, pp. 627–639, 2010.

**Paul M. Moubarak** (S'09) received the Master's degree in mechanical engineering from the University of Maryland, College Park, MD, USA, in 2007, with a thesis focused on bioinstrumentation and signal processing. He is a currently working toward the Ph.D. degree in the Robotics and Mechatronics Laboratory, Department of Mechanical and Aerospace Engineering, The George Washington University, Washington, DC, USA.

His current research interests include basic and applied research in robotics and mechatronics, and involve investigations in mobility and manipulation motion control, dynamical systems, optimization, and algorithms.

**Pinhas Ben-Tzvi** (S'02–M'08–SM'12) received the B.S. degree (*summa cum laude*) in mechanical engineering from the Technion—Israel Institute of Technology, Haifa, Israel, in 2000 and the M.S. and Ph.D. degrees in mechanical engineering from the University of Toronto, Toronto, ON, Canada, in 2004 and 2008, respectively.

He is currently an Assistant Professor in the Department of Mechanical and Aerospace Engineering and the founding Director of the Robotics and Mechatronics Laboratory at The George Washington University, Washington, DC, USA. Before joining the University of Toronto in 2002, he was an R&D Engineer with General Electric Medical Systems Company, developing medical diagnostic robotic and mechatronic systems. His current research interests include robotics and autonomous systems, mechatronics, dynamic systems and control, mechanism/machine design and integration, and sensing and actuation. Applications include autonomous mobile robot mobility and manipulation and modular and reconfigurable mobile robotics for search and rescue, environment monitoring, and defense; active dynamic continuum robotic tails for maneuvering/stabilizing mobile robots; advanced medical devices and robotic systems for surgery and rehabilitation; haptics devices and exoskeletons for robot control and rehabilitation; and novel sensors and actuators for biomedical applications.

Dr. Ben-Tzvi is the recipient of the 2013 GW SEAS Outstanding Young Researcher Award and the GW SEAS Outstanding Young Teacher Award, as well as several other honors and awards. He is a member of the American Society of Mechanical Engineers (ASME).